Chemical Science

ROYAL SOCIETY OF CHEMISTRY

EDGE ARTICLE

View Article Online
View Journal | View Issue

Cite this: *Chem. Sci.*, 2026, **17**, 1859

All publication charges for this article have been paid for by the Royal Society of Chemistry

Programmed intralayer Co and interlayer Ni atoms in a covalent organic framework for synergistic CO_2 photoreduction

Jie-Yu Yue,†*[ab] Rui-Zhi Zhang,†[a] Xi Chen,[c] Chengcheng Liu,[c] Peng Yang *[a] and Bo Tang *[a]

The atom programming of multiple active centers is a central goal in advanced catalysis, yet it remains a formidable challenge, particularly for complex transformations like CO_2 photoconversion that require orchestrated multi-electron/proton pathways. Herein, we report an orthogonal site-encoding strategy, driven by coordination adaptability, that enables unprecedented atomic-level spatial programming within a dual-metal covalent organic framework (TZCOF), featuring precisely positioned intralayer $CoNOCl_2$ and interlayer NiN_2Cl_2 sites. This architecturally programmed CoNi-TZCOF exhibits exceptional performance, with a CO generation rate of 13.6 mmol g^{-1} h^{-1} (98.7% selectivity), significantly outperforming pristine TZCOF (51.6% selectivity), Co-TZCOF (88.5% selectivity), and Ni-TZCOF (85.9% selectivity) by factors of 41.2, 1.3, and 6.2, respectively. Moreover, in simulated flue gas containing 15% CO_2, CoNi-TZCOF also displays excellent CO production activity (12.9 mmol g^{-1} h^{-1}, 96.5% selectivity), demonstrating its potential for industrial applications. Mechanistic investigations reveal a synergistic donor–acceptor interaction wherein the interlayer Ni sites modulate the electronic structure of the intralayer Co active centers, thereby optimizing the d-band center and facilitating the formation of the critical *COOH intermediate. This study establishes a powerful atom programming strategy for bimetallic sites within crystalline materials, paving the way toward designing catalysts with spatially controlled, multi-atomic architectures for complex chemical transformations.

Received 31st October 2025
Accepted 23rd November 2025

DOI: 10.1039/d5sc08435k

rsc.li/chemical-science

Introduction

Although atom editing has made remarkable advances in organic synthesis,[1–3] the spatially precise programmable positioning of diverse single-metal atoms within organic porous material catalysts remains in its infancy. Nature's enzymes represent the pinnacle of catalytic design, orchestrating complex chemical transformations with unparalleled efficiency and selectivity.[4] This sophisticated architecture, which positions metal cofactors and amino acid residues with atomic precision, facilitates site isolation and synergistic catalysis, exemplified by the nitrogenase system (Fig. 1a).[5] Emulating this level of spatial control in synthetic materials remains a grand challenge and a holy grail for chemists, particularly for addressing complex environmental challenges.

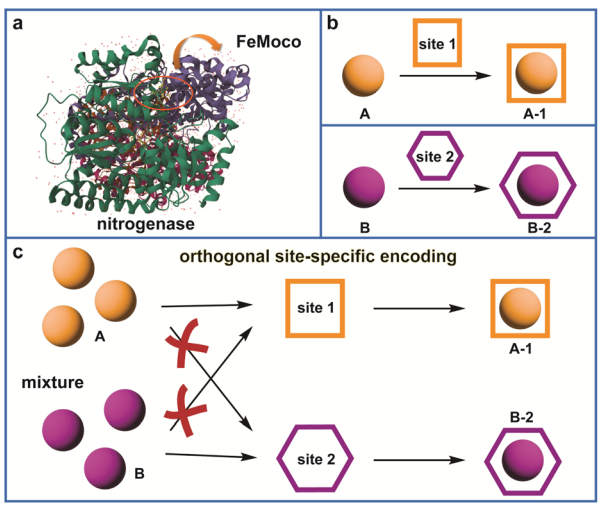

Fig. 1 Schematic diagram of (a) the nitrogenase with FeMoco sites and (b and c) orthogonal site-specific encoding strategy.

[a]*Key Laboratory of Molecular and Nano Probes, Ministry of Education, Collaborative Innovation Center of Functionalized Probes for Chemical Imaging in Universities of Shandong, College of Chemistry, Chemical Engineering and Materials Science, Shandong Normal University, Jinan, 250014, P. R. China. E-mail: yuejieyu@sdnu.edu.cn; yangpeng@sdnu.edu.cn; tangb@sdnu.edu.cn*

[b]*Hubei Key Laboratory of Processing and Application of Catalytic materials, Huanggang Normal University, Huanggang, 438000, P. R. China*

[c]*Institute of Frontier Chemistry, School of Chemistry and Chemical Engineering, Shandong University, Qingdao, 266237, P. R. China*

† These authors contributed equally to this work.

Among these challenges, the photocatalytic CO_2 reduction reaction (PCO_2RR) holds paramount significance for mitigating climate change and meeting sustainable energy demands.[6–11] This approach not only serves to mitigate atmospheric CO_2 concentrations but also facilitates the conversion of CO_2 into value-added chemicals and renewable fuels, thereby enabling carbon valorization and fostering sustainable energy production. Nevertheless, PCO_2RR continues to face formidable challenges pertaining to reaction activity and product selectivity largely attributed to the intricate multi-electron/proton transfer mechanisms and complex intermediate pathways.[12–14] Compounding these difficulties, the undesirable hydrogen evolution reaction (HER) often competes with the CO_2 photoreduction process, leading to compromised selectivity. Consequently, rational design of efficient photocatalysts capable of enhancing PCO_2RR kinetics and modulating product distribution has emerged as a critical strategy.[15]

Covalent organic frameworks (COFs), renowned for their crystalline porous architecture, present an exceptional platform for photocatalytic applications, attributed to their precisely engineered structural motifs, expansive surface area, superior crystallinity, and remarkable chemical and thermal robustness.[16–18] The judicious selection of building blocks and the extensive π-conjugated network permeating throughout both intra- and interlayer domains of COFs facilitate enhanced charge carrier mobility. Moreover, these frameworks serve as ideal scaffolds for anchoring atomically dispersed catalytic centers *via* coordination interactions between metal species and specific functional moieties embedded within the framework.[18–21] The strategic incorporation of atomically dispersed metallic sites enables systematic modulation of the photophysical and electronic properties, directly influencing photocatalytic efficacy.

While metal-coordinated COFs for PCO_2RR have garnered significant scholarly attention, most reported systems employ single-metal active sites, which frequently encounter challenges in CO_2 activation and subsequent transformation processes.[22–30] To overcome these limitations, dual-metal site catalysts (DMCs) have emerged as promising alternatives, offering heterogeneous active centers comprising two catalytic species that can work synergistically.[31–37] These DMCs consistently exhibit superior activity compared to their single-metal counterparts due to their distinctive bimetallic interactions and synergistic coordination configurations.[38,39] This advantage is particularly salient in intricate multi-electron processes, where diverse intermediates necessitate concerted activation by multiple metallic centers. The cooperative effects between distinct metal sites enable precise modulation of electronic structure, augment charge separation, and accelerate multi-electron transfer pathways.[40–42]

Despite this potential, the site-specific programming of two different metal atoms into a COF, that is, placing metal A exclusively at one type of site and metal B at another (Fig. 1b), remains challenging in synthetic chemistry. Current strategies are largely confined to applying metal-contained porphyrin or phthalocyanine as parts of monomers for COF synthesis.[36,43–45] Consequently, while these systems have shown promise, the synergistic mechanisms governing bimetallic catalysis beyond these specific motifs remain poorly understood. A more ambitious frontier is the precise control over the three-dimensional spatial arrangement of these atoms.[46] The ability to create, for example, a heterobimetallic system with one metal atom precisely anchored intralayer and the other exclusively interlayer could pave the way for entirely new catalytic paradigms. However, realizing such atomic-level spatial programming remains a formidable challenge, as it necessitates a sophisticated lock-and-key recognition mechanism.

Herein, by leveraging an orthogonal site-encoding strategy driven by coordination adaptability (Fig. 1c), we successfully constructed a bimetallic TZCOF photocatalyst featuring precisely positioned intralayer $CoNOCl_2$ and interlayer NiN_2Cl_2 sites, in which single Co site was coordinated in the intralayer of TZCOF and single Ni site was coordinated in the interlayer of TZCOF whether Co and Ni sources were added separately or mixed together. Comprehensive characterizations unequivocally confirmed the atomic dispersion of both metal centers and elucidated their distinct, spatially segregated coordination environments. This programming precise CoNi-TZCOF exhibited a remarkable CO generation rate of 13.6 mmol g^{-1} h^{-1} with 98.7% selectivity, significantly outperforming its single-metal counterparts Co-TZCOF, Ni-TZCOF, and pristine TZCOF by factors of 1.3, 6.2, and 41.2, with the CO selectivity of 88.5%, 85.9%, and 51.6%, respectively. Further theoretical calculations revealed the donor–acceptor electronic coupling between the $CoNOCl_2$ and NiN_2Cl_2 moieties, which drives electron transfer from the Ni to the Co centers. While the intralayer $CoNOCl_2$ center was identified as the primary active site for CO_2 reduction, the proximate interlayer NiN_2Cl_2 site synergistically boosted the catalytic performance by optimizing the d-band center and lowering the energy barrier for the crucial *COOH formation on the Co center. This work provides fundamental insights into the synergistic mechanisms within dual-metal COF photocatalysts. More importantly, our orthogonal site-encoding approach enables the programmable arrangement of multicomponent active sites with atomic precision, offering a compelling avenue for the design and fabrication of catalysts for complex chemical transformations.

Results and discussion

The structural design was exhibited in Fig. 2a. A novel thiadiazole-based TZCOF with cpt topology was synthesized *via* a [6 + 2] condensation, applying 4′,4‴,4⁗⁗-(1,3,5-triazine-2,4,6-triyl)tris([1,1′-biphenyl]-3,5-dicarbaldehyde)) (TBD) and 4,4′-(benzo[*c*][1,2,5]thiadiazole-4,7-diyl)dianiline (BTZ) as monomers. The pristine TZCOF was then subjected to post-synthetic metalation using $CoCl_2 \cdot 6H_2O$ and $NiCl_2 \cdot 6H_2O$ to afford three distinct metal-incorporated variants: Co-TZCOF, Ni-TZCOF, and the bimetallic CoNi-TZCOF.

The crystalline structures of TZCOF, Co-TZCOF, Ni-TZCOF, and CoNi-TZCOF were manifested by powder X-ray diffraction (PXRD) analysis. Fig. 2b presented the experimental PXRD pattern of the TZCOF alongside the simulated patterns derived from both AA and AB stacking models. The experimental PXRD profiles of TZCOF exhibited characteristic peaks at 1.87°, 5.23°,

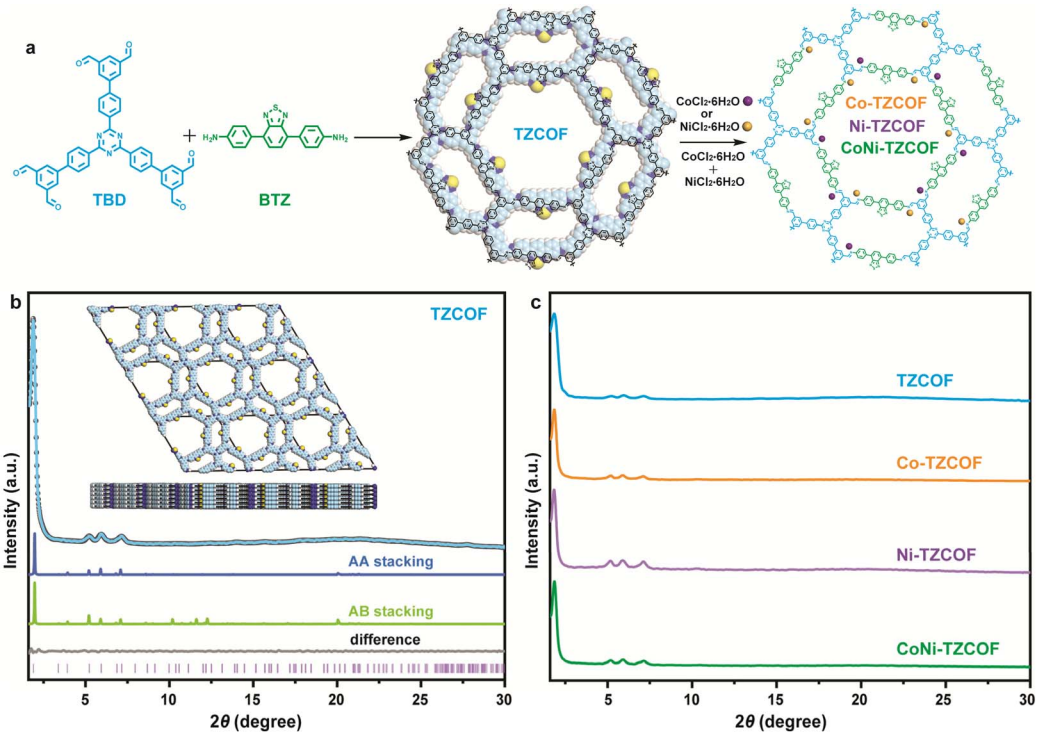

Fig. 2 (a) Chemical structures of TZCOF, Co-TZCOF, Ni-TZCOF, and CoNi-TZCOF. (b) Experimental and simulated PXRD profiles of TZCOF. (c) PXRD patterns of Co-TZCOF, Ni-TZCOF, and CoNi-TZCOF.

5.95°, 7.12°, and about 25°, assigned to the (100), (210), (300), (310), and (001) planes, respectively. The experimental PXRD curve of TZCOF aligned well with the simulated pattern of the AA stacking model. The unit cell parameters of TZCOF were $a = b = 51.90$ Å, $c = 3.52$ Å, $\alpha = \beta = 90°$, and $\gamma = 120°$, with refinement factors of $R_{wp} = 2.40\%$ and $R_p = 1.81\%$. Following metalation, the crystallinity of the frameworks was preserved, as evidenced by the PXRD patterns of Co-TZCOF, Ni-TZCOF, and CoNi-TZCOF shown in Fig. 2c. All metal-incorporated frameworks retained the characteristic diffraction peaks of the parent TZCOF (1.87°, 5.23°, 5.95°, 7.12°, and about 25°), albeit with slight intensity variations attributable to the introduction of metal centers within the skeletons. The structural integrity maintained after metalation highlighted the robustness of TZCOF and its suitability as a platform for incorporating diverse metal centers. Co-TZCOF, Ni-TZCOF, and CoNi-TZCOF were ideal candidates for investigating structure–property relationships in dual-metal catalytic systems for PCO_2RR, particularly the synergistic effects between different metal centers within a single framework.

Analysis of the solid-state ^{13}C NMR spectra of TZCOF (Fig. S1) revealed characteristic chemical shifts at 169.51, 153.62, and 150.55 ppm, attributed to the carbon atoms in the triazine, imine, and thiadiazole modules of TZCOF, respectively. In addition, the Fourier transform infrared spectra (FT-IR) of the as-synthesized four COFs were collected in Fig. S2. TZCOF showed new vibration peaks at 1623 cm^{-1}, belonging to the signals of the imine linkage; those in Co-TZCOF, Ni-TZCOF, and CoNi-TZCOF were 1621 cm^{-1}.

To fully understand the properties of TZCOF, Co-TZCOF, Ni-TZCOF, and CoNi-TZCOF, we conducted N_2 sorption analysis. As exhibited in Fig. 3a and b, the Brunauer–Emmett–Teller (BET) surface areas of TZCOF, Co-TZCOF, Ni-TZCOF, and CoNi-TZCOF were 1276, 1126, 1173, and 1050 $m^2\ g^{-1}$, respectively. After metal ions incorporation, the BET surface areas of Co-TZCOF, Ni-TZCOF, and CoNi-TZCOF were reduced compared to pristine TZCOF. The major pore diameters of TZCOF were 1.80 and 3.41 nm, those of Co-TZCOF (1.74 and 3.39 nm), Ni-TZCOF (1.78 and 3.40 nm), and CoNi-TZCOF (1.73 and 3.36 nm) were little reduced, confirming that metal incorporation occurred without significant structural collapse or pore blockage.

X-ray photoelectron spectroscopy (XPS) was utilized to elucidate the chemical states and coordination environments of the incorporated metal centers. The high-resolution Co 2p spectra of CoNi-TZCOF (Fig. 3c) exhibited two characteristic peaks at 782.47 and 797.50 eV, corresponding to Co $2p_{3/2}$ and Co $2p_{1/2}$, respectively. Analogously, the Ni 2p spectra (Fig. 3c) manifested peaks at 856.81 and 874.31 eV, ascribed to Ni $2p_{3/2}$ and Ni $2p_{1/2}$, respectively. The aforementioned binding energies were consistent with Co^{2+} and Ni^{2+} species.[47,48] Furthermore, in comparison to the N 1s binding energies in TZCOF at 399.99, 399.21, and 398.90 eV, belonging to the N species in the triazine, thiadiazole, and imine modules, respectively, in Fig. 3d, the shifted peak position in CoNi-TZCOF at 398.57 eV demonstrated the coordination of metal ions with the N atoms in imine bonds.[49,50] Notably, the binding energies of S 2p in Fig. 3e exhibited no significant alterations in TZCOF and CoNi-TZCOF.

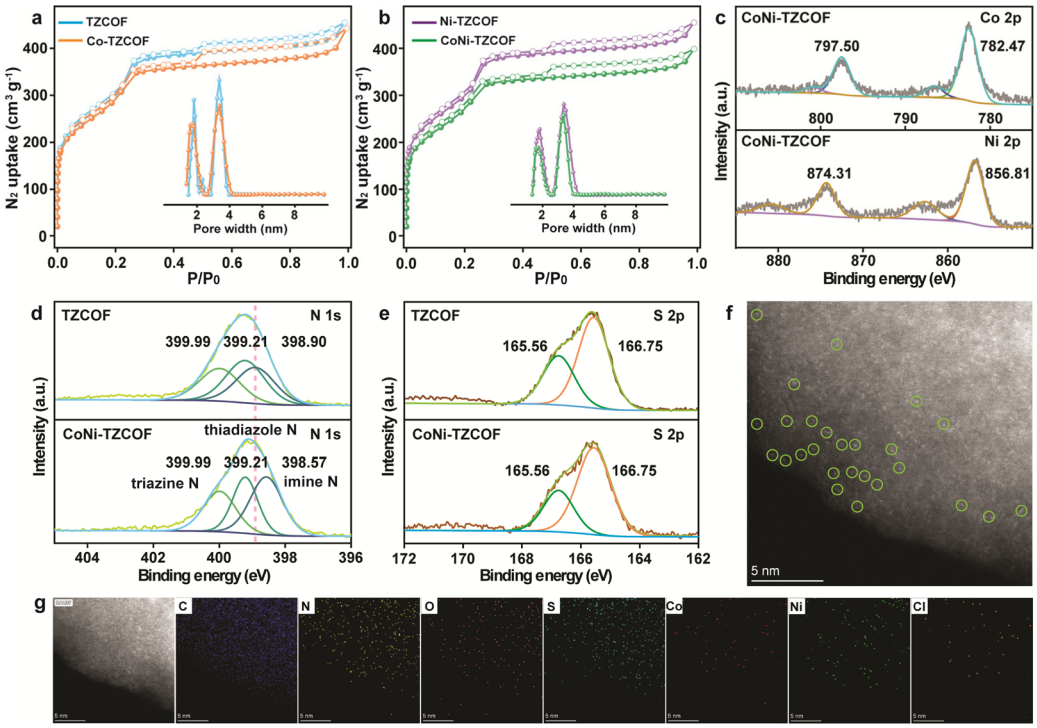

Fig. 3 N_2 sorption isotherms and pore size distribution curves of (a) TZCOF, Co-TZCOF, (b) Ni-TZCOF, CoNi-TZCOF. (c) High-resolution Co 2p and Ni 2p XPS spectra of CoNi-TZCOF. (d) High-resolution N 1s XPS spectra of TZCOF and CoNi-TZCOF. (e) High-resolution S 2p XPS spectra of TZCOF and CoNi-TZCOF. (f) The AC-HAADF-STEM image of CoNi-TZCOF. (g) Elemental mapping images of CoNi-TZCOF.

The disparities in XPS spectra between TZCOF and CoNi-TZCOF corroborated that Co and Ni ions were coordinated with the N atoms from the imine bond in TZCOF.[49,50]

Moreover, the high-resolution XPS spectra of Co 2p, N 1s, and S 2p in Co-TZCOF and Ni-TZCOF were acquired and presented in Fig. S3, respectively. In both Co-TZCOF and Ni-TZCOF, Co and Ni ions were unequivocally coordinated with the N atoms from the imine bond in TZCOF. Remarkably, XPS analysis revealed that the peaks corresponding to Co $2p_{1/2}$ and Co $2p_{3/2}$ in CoNi-TZCOF were shifted negatively by 0.24 and 0.23 eV, respectively, in comparison to those of Co-TZCOF. Conversely, the Ni $2p_{1/2}$ and Ni $2p_{3/2}$ peaks in CoNi-TZCOF were shifted positively by 0.35 and 0.30 eV, respectively, when compared to the Ni-TZCOF. These observations suggested electronic coupling between the Co and Ni species within CoNi-TZCOF.

Morphological investigations of TZCOF, Co-TZCOF, Ni-TZCOF, and CoNi-TZCOF were performed using scanning and high-resolution transmission electron microscopy (SEM and HRTEM). The as-synthesized four COFs all showed coral-like morphologies with distinct surface protrusions in Fig. S4, indicating that the incorporation of Co and Ni ions did not induce appreciable alterations in the structural topography. Additionally, the HRTEM images with lattice fringes related to the (100) plane of TZCOF, Co-TZCOF, Ni-TZCOF, and CoNi-TZCOF were displayed in Fig. S5, corroborating their good crystallinity. The distribution of isolated Co and Ni atoms was elucidated through aberration-corrected high-angle annular dark-field scanning transmission electron microscopy (AC-HAADF-STEM). As depicted in Fig. 3f, individual Co and Ni atoms were unequivocally discernible as discrete bright spots within the CoNi-TZCOF. These discrete locations were further accentuated by green circles in the corresponding micrograph. Furthermore, energy-dispersive spectroscopy (EDS) elemental mapping images of CoNi-TZCOF substantiated the homogeneous distribution of C, N, O, S, Co, Ni, and Cl elements throughout the backbones of CoNi-TZCOF, as depicted in Fig. 3g. The metal contents of Co and Ni in CoNi-TZCOF were determined by inductively coupled plasma spectrometry (ICP), yielding values of 1.33 wt% and 1.46 wt%, respectively, corresponding to a Co : Ni ratio of approximately 1 : 1.1. For the individual Co-TZCOF and Ni-TZCOF samples, the Co and Ni contents were 1.40 wt% and 1.52 wt%, respectively.

To elucidate the precise coordination environments of the Co and Ni centers in CoNi-TZCOF, we conducted comprehensive X-ray absorption fine structure (XAFS) analyses. The Co K-edge X-ray absorption near-edge structure (XANES) spectra of CoNi-TZCOF, Co foil, Co_3O_4, CoO, and CoPc were exhibited in Fig. 4a. The absorption edge position of CoNi-TZCOF was close to that of CoO and CoPc, manifesting that Co species in CoNi-TZCOF existed principally in the +2 oxidation state, in accordance with the Co 2p XPS spectra in Fig. 3c. The corresponding Fourier-transformed extended X-ray absorption fine structure (EXAFS) spectra (Fig. 4b) revealed prominent peaks at approximately 1.8 Å and 2.4 Å, which can be attributed to Co–N/O and Co–Cl coordination spheres, respectively.[22,26] Notably, the

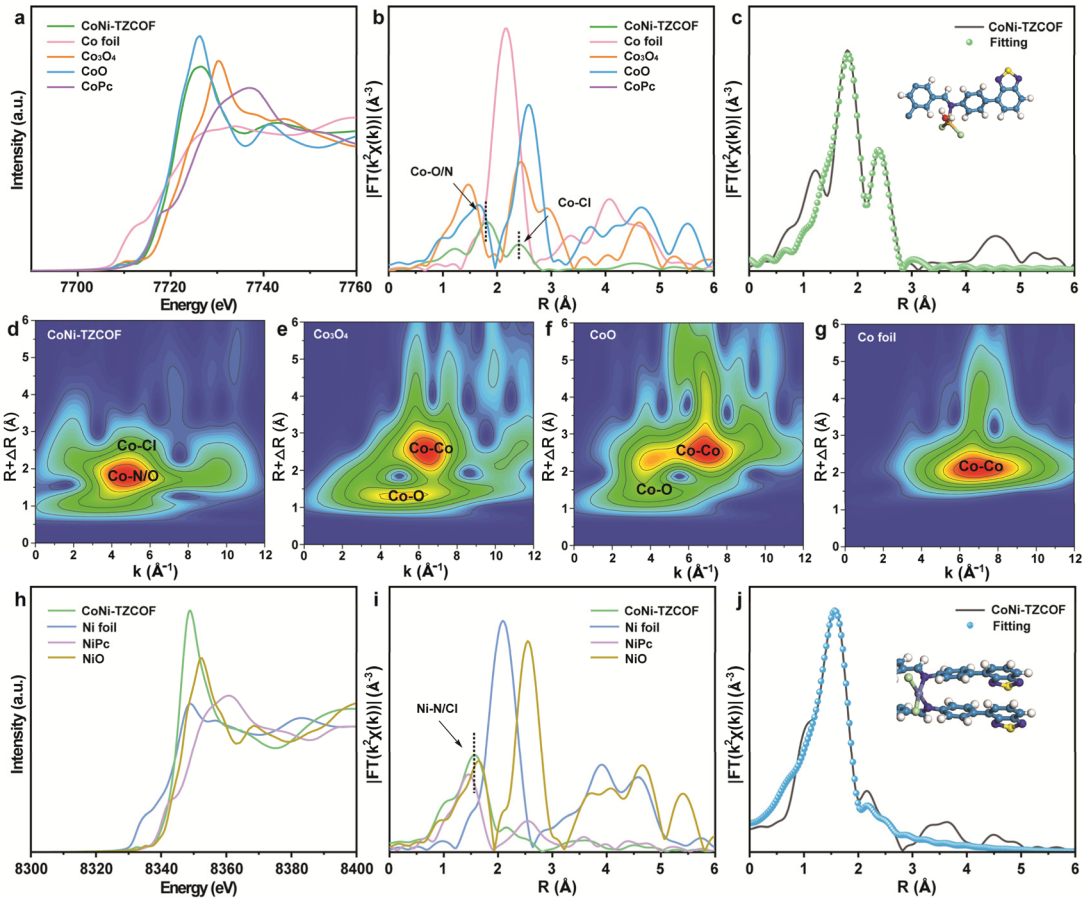

Fig. 4 Co K-edge (a) XANES spectra and (b) EXAFS spectra of CoNi-TZCOF, Co foil, Co_3N_4, CoO, and CoPc. (c) Co K-edge EXAFS fitting curves of CoNi-TZCOF. Co K-edge WT-EXAFS contour plots of (d) CoNi-TZCOF, (e) Co_3N_4, (f) CoO, and (g) Co foil. Ni K-edge (h) XANES spectra and (i) EXAFS spectra of CoNi-TZCOF, Ni foil, NiO, and NiPc. (j) Ni K-edge EXAFS fitting curves of CoNi-TZCOF.

absence of peaks at 2.2 Å confirmed the lack of Co–Co interactions, providing compelling evidence for the atomic dispersion of Co sites in CoNi-TZCOF. Quantitative EXAFS fitting (Fig. 4c) further corroborated this coordination environment, revealing that each Co atom was coordinated with one N atom, one O atom, and two Cl atoms, resulting in an intralayer $CoNOCl_2$ configuration (Table S1). Further wavelet transform (WT) analysis of the Co K-edge EXAFS in CoNi-TZCOF, Co_3N_4, CoO, and Co foil (Fig. 4d–g) disclosed spatial resolution of Co–N/O and Co–Cl paths and the absence of Co–Co paths in CoNi-TZCOF. The related color scale bars for Fig. 4d–g were SI in Fig. S6.

Parallel analyses were conducted for the Ni K-edge of CoNi-TZCOF. The XANES spectra (Fig. 4h) of CoNi-TZCOF exhibited features distinct from Ni foil but close to NiPc and NiO references, indicating an oxidation state of +2 for the Ni species in CoNi-TZCOF. The corresponding EXAFS spectra (Fig. 4i) displayed a prominent peak at approximately 1.57 Å, attributed to Ni–N/Cl coordination.[51] EXAFS fitting curves in Fig. 4j revealed that each Ni atom was coordinated with two N atoms and two Cl atoms in an interlayer NiN_2Cl_2 configuration (Table S2). The WT analysis of Ni K-edge EXAFS alongside reference spectra (Fig. S7) indicated distinct Ni–N/Cl coordination environments. Furthermore, the complete absence of Ni–Ni scattering contributions was observed for CoNi-TZCOF, confirming the atomically dispersed Ni species in CoNi-TZCOF. The above characterizations proved the complementary coordination environments of Co and Ni atoms in CoNi-TZCOF, establishing a bimetallic system featuring atomically dispersed intralayer $CoNOCl_2$ and interlayer NiN_2Cl_2 sites. This unique dual-metal arrangement created synergistic electronic effects that we anticipate will significantly enhance the PCO_2RR performance through optimized electronic structures and intermediate binding energetics.

Additionally, the XAFS spectra of single-metal Co-TZCOF and Ni-TZCOF were collected in Fig. S8 and 9 with EXAFS fitting parameters in Tables S3 and 4. These findings demonstrated that in Co-TZCOF, each Co atom was coordinated with one N atom, one O atom, and two Cl atoms, forming an intralayer $CoNOCl_2$ configuration; in Ni-TZCOF, each Ni atom was coordinated with two N atoms and two Cl atoms, resulting in an interlayer NiN_2Cl_2 configuration. Interestingly, regardless of whether $CoCl_2 \cdot 6H_2O$ and $NiCl_2 \cdot 6H_2O$ were introduced to the TZCOF framework separately or simultaneously, the single Co sites invariably occupied intralayer positions, whereas the single Ni sites consistently coordinated in the interlayer space,

indicating the two processes were mutually independent. The coordination of Co and Ni sites within TZCOF proceeded orthogonally in the intralayer and interlayer, which was rare.[21] We postulated that the distinct coordination modes exhibited by the single Co site and single Ni site within the TZCOF skeleton were driven by coordination adaptability, which stemmed from their intrinsic coordination chemistry characteristics, the structural features of the COF, and the specific interactions between the metal ions and the COF scaffold.[52,53] Furthermore, we calculated and compared the energies of bimetallic TZCOF with other Co/Ni coordination styles, such as interlayer Co/intralayer Ni, intralayer Co/Ni, and interlayer Co/Ni (Fig. S10). The obtained TZCOF with intralayer Co/interlayer Ni was the more thermodynamically stable product.

Besides, thermogravimetric analysis (TGA) was employed to elucidate the thermal stability profiles of the as-synthesized four COFs. As illustrated in Fig. S11, TZCOF, Co-TZCOF, Ni-TZCOF, and CoNi-TZCOF all exhibited good thermal robustness. Moreover, PXRD analyses (Fig. S12) demonstrated that all four COFs maintained their crystalline integrity following immersion in a spectrum of solvents, thus substantiating their resistance to solvolytic degradation.

The optical and electronic properties of the pristine and metal-incorporated COFs were investigated. The UV-visible diffuse reflectance spectra (UV-vis DRS) of TZCOF, Co-TZCOF, Ni-TZCOF, and CoNi-TZCOF were presented in Fig. 5a. The pristine TZCOF exhibited strong absorption in the visible light region with an absorption edge extending to approximately 550 nm. Upon metal incorporation, Co-TZCOF, Ni-TZCOF, and CoNi-TZCOF displayed enhanced visible light absorption ranges. The corresponding Tauc plots (inset of Fig. 5a) revealed optical bandgaps of 2.17, 2.14, 2.06, and 2.09 eV for TZCOF, Co-TZCOF, Ni-TZCOF, and CoNi-TZCOF, respectively.

Examination of the Mott–Schottky analyses (Fig. S13) revealed positive slopes for all four synthesized COFs, definitively establishing their n-type semiconducting nature. The corresponding flat band potentials were ascertained to be −0.80, −0.58, −0.57, and −0.68 V (*vs.* Ag/AgCl) for TZCOF, Co-TZCOF, Ni-TZCOF, and CoNi-TZCOF, respectively. The energy band architectures were acquired through comprehensive analysis of optical bandgaps and flat-band potentials to elucidate their redox capabilities (Fig. 5b). The conduction band (CB) potentials were determined to be −0.90, −0.68, −0.67, and −0.78 V (*vs.* NHE) for TZCOF, Co-TZCOF, Ni-TZCOF, and CoNi-TZCOF, respectively, all exhibiting more negative values than the requisite CO_2/CO reduction potential (−0.53 V *vs.* NHE),[54] thereby demonstrating thermodynamic favorability for CO_2 reduction.

Photoluminescence (PL) spectroscopic investigations further explicated the charge carrier dynamics of TZCOF, Co-TZCOF, Ni-TZCOF, and CoNi-TZCOF (Fig. 5c). The bimetallic CoNi-TZCOF exhibited markedly diminished PL intensities relative to its analogues, indicative of enhanced charge separation efficiency and suppressed electron–hole recombination. Time-resolved PL decay measurements (Fig. 5d) corroborated these observations (calculation details were displayed in SI), with CoNi-TZCOF (3.43 ns) demonstrating prolonged average fluorescence lifetimes compared to pristine TZCOF (1.41 ns), Co-TZCOF (2.00 ns), and Ni-TZCOF (1.94 ns), substantiating the enhancement of charge transfer processes through dual metal ions incorporation. Notably, CoNi-TZCOF exhibited superior charge transfer efficiency compared to its single-metal counterparts.

Transient photocurrent response measurements (Fig. 5e) revealed prompt and reproducible photocurrent generation under intermittent illumination for all synthesized COFs,

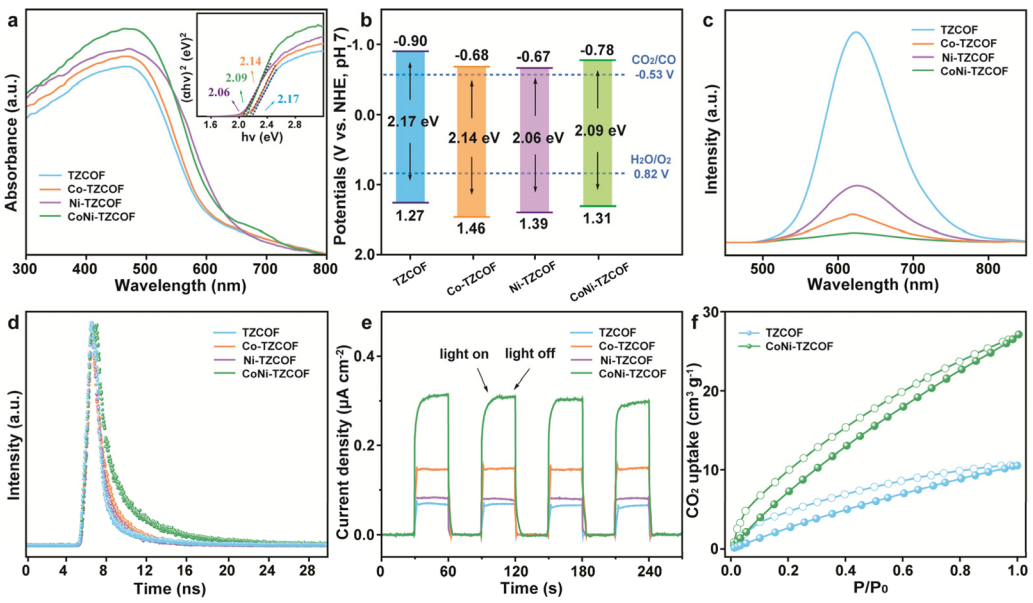

Fig. 5 (a) The UV-vis DRS with Tauc plots, (b) the energy band structures, (c) the PL spectra, (d) time-resolved PL spectra, (e) photocurrent density of TZCOF, Co-TZCOF, Ni-TZCOF, and CoNi-TZCOF. (f) CO_2 uptake capability of TZCOF and CoNi-TZCOF at 273 K.

confirming their photoresponsive characteristics. CoNi-TZCOF displayed preeminent photocurrent density, followed sequentially by Co-TZCOF, Ni-TZCOF, and TZCOF. Electrochemical impedance spectroscopic (EIS) investigations, manifested in Nyquist plots (Fig. S14), revealed substantially reduced semicircle radii for CoNi-TZCOF relative to Co-TZCOF, Ni-TZCOF, and TZCOF, indicating significantly diminished charge transfer resistance after Co and Ni co-modification.

Moreover, CO_2 adsorption characteristics were evaluated through sorption isotherms at 273 K (Fig. 5f). CoNi-TZCOF demonstrated markedly enhanced CO_2 uptake (approximately 27.1 $cm^3\ g^{-1}$) compared to the pristine TZCOF (10.5 $cm^3\ g^{-1}$), indicating that dual metal coordination essentially augmented the CO_2 affinity. This remarkable enhancement can be attributed to the presence of coordinative metal sites that served as preferential binding sites for CO_2 molecules through Lewis acid–base interactions.[55] The significantly improved CO_2 adsorption capacity of CoNi-TZCOF provided a higher local concentration of CO_2 around the catalytic centers. The optimized electronic structure and superior charge separation efficiency provided mechanistic insights into the exceptional PCO_2RR performance exhibited by CoNi-TZCOF.

The PCO_2RR performances of the judiciously designed TZCOF, Co-TZCOF, Ni-TZCOF, and CoNi-TZCOF were systematically evaluated under visible light irradiation, utilizing $[Ru(bpy)_3]Cl_2\cdot 6H_2O$ as the photosensitizer and triethanolamine (TEOA) as the sacrificial agent. Gaseous and liquid products were analyzed through gas chromatography (GC) and ^1H NMR spectroscopy, respectively. The findings indicated that, aside from the targeted CO, no characteristic signals attributable to methanol, ethanol, and formic acid were detected (Fig. S15). Initial investigations focused on dissecting the catalytic contributions of the TZCOF backbone and the incorporated single metal and bimetal sites. As depicted in Fig. 6a, the pristine TZCOF exhibited minimal PCO_2RR activity, producing negligible amounts of both CO (0.33 mmol $g^{-1}\ h^{-1}$) and H_2 (0.31 mmol $g^{-1}\ h^{-1}$), which underscored the limited intrinsic photocatalytic capability of the bare TZCOF skeleton. Upon the introduction of single-metal sites, Co-TZCOF and Ni-TZCOF demonstrated significantly enhanced CO production rates of 10.8 and 2.2 mmol $g^{-1}\ h^{-1}$, respectively, indicating the activation of CO_2 by the coordinated metal centers. The CO formation selectivity on Co-TZCOF and Ni-TZCOF was 88.5% and 85.9%, respectively. Notably, the CoNi-TZCOF, integrating atomically dispersed intralayer $CoNOCl_2$ and interlayer NiN_2Cl_2 moieties, achieved the highest CO production rate (13.6 mmol $g^{-1}\ h^{-1}$) and CO selectivity (98.7%) among the four as-synthesized COFs. The CO production rate of CoNi-TZCOF was much higher than that of the single-metal counterparts, Co-TZCOF and Ni-TZCOF, as well as the original TZCOF, being 1.3, 6.2, and 41.2 times greater, respectively. Moreover, the CO_2RR activity of the physically mixed Co-TZCOF and Ni-TZCOF (the mass ratio was 1 : 1) was explored, which was 6.4 mmol $g^{-1}\ h^{-1}$ with the selectivity of 71.1%. CoNi-TZCOF displayed enhanced photocatalytic activity compared to the physically mixed Co-TZCOF and Ni-TZCOF, proving the synergistic effects between the Co and Ni sites.

In addition, the apparent quantum efficiencies (AQE) for TZCOF, Co-TZCOF, Ni-TZCOF, and CoNi-TZCOF were found to be 0.23%, 1.16%, 2.07%, and 4.17%, respectively, when measured at 420 nm. That of CoNi-TZCOF was comparable to the reported data in Table S5. Furthermore, the turnover number (TON) for CO production was assessed to be 130.5, 82.8, and 14.5 for CoNi-TZCOF, Co-TZCOF, and Ni-TZCOF, respectively, revealing an increased value in bimetallic CoNi-TZCOF.[56,57] A comparative analysis with TZCOF, Co-TZCOF, and Ni-TZCOF revealed the superior PCO_2RR activity and selectivity of CoNi-TZCOF, which strongly indicated a significant synergistic interaction between the co-incorporated Co and Ni active sites. This collective behavior demonstrably enhanced CO_2 photoreduction efficiency beyond that observed with individual metal centers. Comparisons of the CO evolution rate and selectivity of CoNi-TZCOF and other COF-based photocatalysts were listed in Table S5.

The temporal evolution of CO further elucidated the stability and sustained activity of these catalysts (Fig. 6b). Over consistent 4 h, bimetallic CoNi-TZCOF consistently showed the highest cumulative CO yield compared to Co-TZCOF, Ni-TZCOF, and TZCOF. Significantly, recyclability experiments involving CoNi-TZCOF indicated no obvious decreases in catalytic activity after five cycles for 10 h (Fig. S16) with little metal loss (Co: 1.24 wt%; Ni: 1.39 wt%). Subsequent analyses, including the PXRD pattern (Fig. S17a), FT-IR spectra (Fig. S17b), XPS spectra (Fig. S18), TEM (Fig. S19), and AC-HAADF-STEM image (Fig. S20) performed on the recovered CoNi-TZCOF following the cycling tests. This highlighted the robust photostability and long-term catalytic efficiency of the CoNi-TZCOF, a critical attribute for practical photocatalytic applications.

To clarify the critical parameters influencing the PCO_2RR activities of CoNi-TZCOF, a series of controlled experiments were systematically conducted (Fig. 6c). As anticipated, the absence of key reaction components, such as light irradiation, CO_2 feedstock, photosensitizer, or sacrificial agent, resulted in negligible CO production, unequivocally confirming their indispensable roles in driving the PCO_2RR. Mechanistic elucidation was further advanced through photoluminescence quenching experiments (Fig. S21), revealing effective photoinduced electron transfer between the photoexcited $[Ru(bpy)_3]Cl_2\cdot 6H_2O$ and CoNi-TZCOF backbone. Optimization of the reaction medium composition demonstrated the complementary functions of water as a proton donor and acetonitrile as a CO_2 solubility enhancer, establishing their synergistic contribution to the catalytic system.

Furthermore, competitive reactions conducted solely with $CoCl_2\cdot 6H_2O$ and $NiCl_2\cdot 6H_2O$, the metal precursors used for incorporation, yielded only trace amounts of CO, H_2, and low selectivity. This critical finding provided compelling evidence that the exceptional catalytic activity observed for CoNi-TZCOF was derived from the atomically dispersed and structurally integrated Co and Ni sites within the TZCOF. Moreover, systematic variation of Co/Ni loading on TZCOF was performed to examine its influence on PCO_2RR performance. The CO_2 reduction activity of CoNi-TZCOF demonstrated a volcano-shaped relationship with the metal content, whereby catalytic

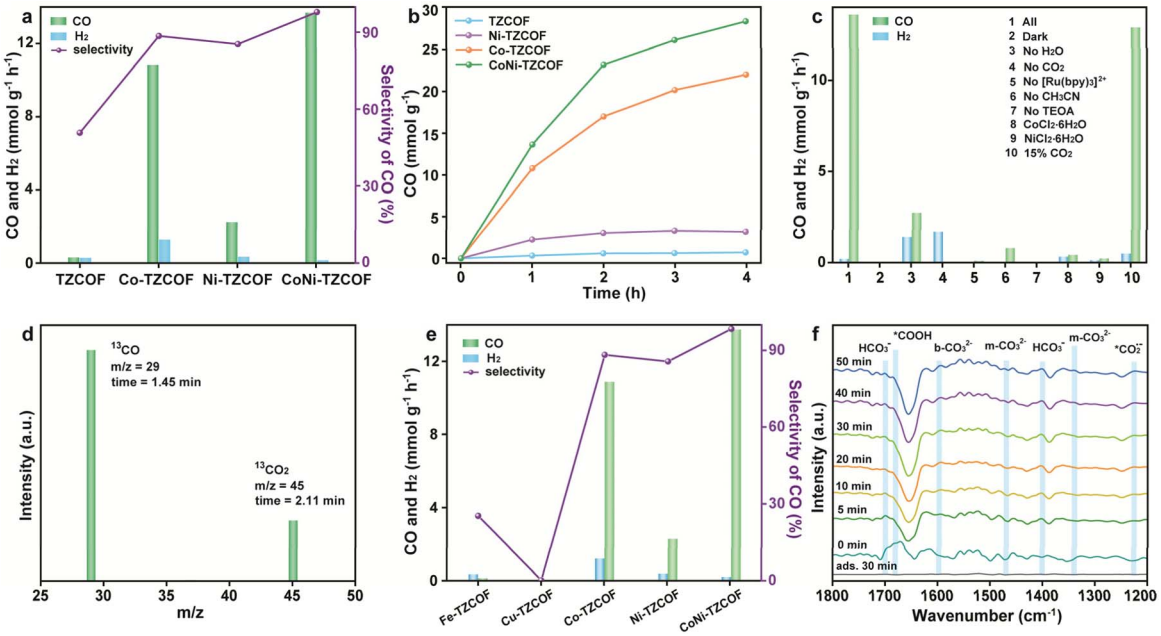

Fig. 6 (a) CO and H_2 evolution rates along with CO selectivity for TZCOF, Co-TZCOF, Ni-TZCOF, and CoNi-TZCOF. (b) Time-dependent CO photoreduction amount over TZCOF, Co-TZCOF, Ni-TZCOF, and CoNi-TZCOF. (c) PCO_2RR activity of CoNi-TZCOF under different reaction conditions, including control experiments with $CoCl_2 \cdot 6H_2O$ and $NiCl_2 \cdot 6H_2O$. (d) GC-MS spectral analysis of $^{13}CO_2$ photoreduction catalyzed by CoNi-TZCOF. (e) Photocatalytic performance evaluation of various metal-incorporated TZCOF (M = Fe, Cu, Co, and Ni) for CO and H_2 production. (f) *In situ* DRIFTS measurements of CoNi-TZCOF during PCO_2RR at various irradiation time intervals.

efficiency initially enhanced and subsequently diminished with increasing metal incorporation (Fig. S22). The subsequent decrease in performance was presumably due to a loss of single-atom dispersion at higher metal loadings, leading to the formation of less active metal nanoclusters.

Crucially, when tested in a simulated flue gas environment consisting of 15% CO_2 and 85% N_2, CoNi-TZCOF demonstrated a CO evolution rate of 12.9 mmol g^{-1} h^{-1}, with the selectivity of 96.5%. This rate surpassed that of Co-TZCOF and Ni-TZCOF by factors of 1.8 and 18.7, respectively. Isotopic labeling experiments were performed using $^{13}CO_2$ as the carbon feedstock to definitively ascertain the carbon source (Fig. 6d). Gas chromatography-mass spectrometry (GC-MS) analysis of the gaseous products revealed a distinct peak at $m/z = 29$, corresponding specifically to ^{13}CO. This result conclusively demonstrated that the produced CO originated directly from the photoreduction of the CO_2 feed. To elucidate the impact of various metal centers on PCO_2RR performance, we incorporated alternative transition metals (Fe and Cu) into the TZCOF, generating Fe-TZCOF and Cu-TZCOF. As exhibited in Fig. 6e, Fe-TZCOF preferred H_2 evolution reaction (HER) and Cu-TZCOF showed almost no activity toward PCO_2RR and HER.

To gain mechanistic insights into the PCO_2RR over CoNi-TZCOF, *in situ* diffuse reflectance infrared Fourier transform spectroscopy (DRIFTS) measurements were conducted under varying illumination durations (Fig. 6f). With increasing illumination time, a distinct and progressively intensifying peak emerged at approximately 1224 and 1684 cm^{-1}, which was characteristic of the $*CO_2^{\cdot-}$ and *COOH intermediates, respectively.[23] Additionally, characteristic vibrational frequencies associated with carbonate functionalities (monodentate CO_3^{2-} centered at 1340 and 1473 cm^{-1}; bidentate CO_3^{2-} at 1594 cm^{-1}) alongside bicarbonate intermediates ($*HCO_3^-$ manifesting at 1403 and 1702 cm^{-1}) emerged during photocatalytic reactions, likely resulting from the aqueous dissolution of CO_2.[28,34,58]

Density functional theory (DFT) calculations were employed to investigate the influence of the atomically dispersed $CoNOCl_2$ and NiN_2Cl_2 constructures within CoNi-TZCOF on its superb PCO_2RR performance. The calculated density of states (DOS) for CoNi-TZCOF, Co-TZCOF, and Ni-TZCOF were presented in Fig. 7a–c. Compared to the single metal Co-TZCOF and Ni-TZCOF, the involvement of $CoNOCl_2$ and NiN_2Cl_2 constructures modulated both the CB and VB distributions of CoNi-TZCOF. Generally, a d-band center positioned closer to the Fermi level is associated with enhanced electron delocalization and promotes catalytic reactivity. Our calculations revealed d-band center positions relative to the Fermi level for CoNi-TZCOF, Co-TZCOF, and Ni-TZCOF to be −1.161 eV (Co center), −1.482 eV (Co center), and 1.258 eV (Ni center), respectively. Notably, the d-band center of CoNi-TZCOF resided considerably closer to the Fermi level than the individual Co-TZCOF and Ni-TZCOF. This upward shift of the Co d-band center in CoNi-TZCOF was understood to reduce the occupancy of antibonding states, thereby strengthening the binding affinity to active intermediates.[59,60] The above evidence indicated that the bimetal Co and Ni sites collaboratively modulated

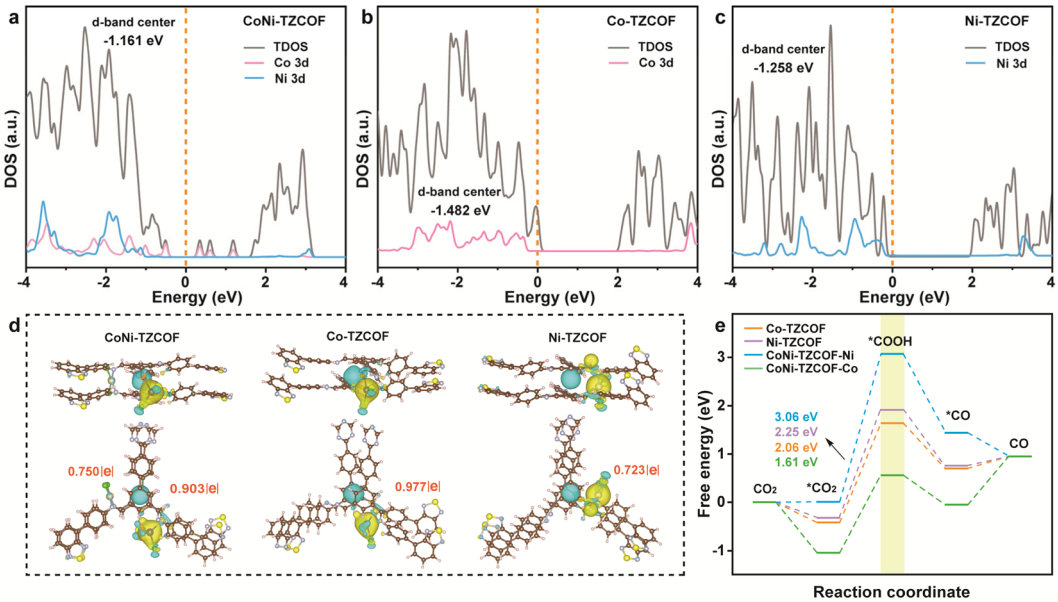

Fig. 7 The DOS of (a) CoNi-TZCOF, (b) Co-TZCOF, and (c) Ni-TZCOF. (d) The charge density difference and Bader charge of CoNi-TZCOF, Co-TZCOF, and Ni-TZCOF (yellow: charge accumulation; blue: charge depletion). (e) Gibbs free energy profiles of the PCO_2RR paths over Co-TZCOF, Ni-TZCOF, Co site in CoNi-TZCOF, and Ni site in CoNi-TZCOF.

the electronic structures and were more favorable for CO_2 activation.

Furthermore, electronic coupling between the $CoNOCl_2$ and NiN_2Cl_2 moieties within CoNi-TZCOF was indicated by observed changes in their charge densities (Fig. 7d). In CoNi-TZCOF, charges were mainly accumulated around the Co center. The robust electron interaction between Co and Ni was further elucidated by Bader charge analysis, which demonstrated a charge inflow of $0.074|e|$ at the Co site upon Ni doping, alongside an increase of $0.027|e|$ in positive charge at the Ni site attributed to the presence of Co atoms, relative to the individual Co-TZCOF or Ni-TZCOF. The above quantitative analysis of charge accumulation on Co and Ni atoms within CoNi-TZCOF revealed the donor–acceptor structure, indicating electron transfer from Ni to Co sites. These findings were consistent with previous XPS results. The increased electron density localized at the Co sites in CoNi-TZCOF was expected to facilitate nucleophilic attack on CO_2.[61]

The PCO_2RR pathways and associated reaction energetics were comprehensively explored by calculating the Gibbs free energy profiles (Fig. 7e). The formation of the *COOH intermediate was the rate-determining step (RDS) in the CO_2 to CO conversion pathway of CoNi-TZCOF, Co-TZCOF, and Ni-TZCOF. Our calculations strikingly demonstrated the catalytic advantage of the dual-metal system. The energy barrier for *COOH formation on the Co site within CoNi-TZCOF was 1.61 eV, a substantial reduction compared to those observed on the Co site in Co-TZCOF (2.06 eV), Ni site in Ni-TZCOF (2.25 eV), and Ni site in CoNi-TZCOF (3.06 eV), respectively. These pronounced reductions in energy barriers clearly illustrated a potent synergistic effect stemming from the intralayer $CoNOCl_2$ and interlayer NiN_2Cl_2 constructures. The co-presence of Co and Ni centers within TZCOF collectively optimized the electronic landscape, thereby facilitating the CO_2 activation step, RDS, and accelerating the overall reaction kinetics. The lowest energy barrier in the RDS in CoNi-TZCOF directly accounted for the significantly enhanced CO_2 reduction activity observed experimentally, underscoring that the atomically dispersed $CoNOCl_2$ and NiN_2Cl_2 motifs synergistically optimized both the electronic properties and catalytic pathways for superior PCO_2RR performance. The proposed PCO_2RR mechanism on CoNi-TZCOF was illustrated in Fig. S23.

Conclusions

To address the challenge of precise spatial regulation of multi-atomic catalytic sites, we developed a coordination-driven orthogonal site-encoding strategy that achieves atomic-precise spatial programming in bimetallic TZCOF, featuring well-defined intralayer $CoNOCl_2$ and interlayer NiN_2Cl_2 sites. This programmable CoNi-TZCOF structure exhibited exceptional catalytic efficacy with a CO evolution rate of 13.6 mmol g^{-1} h^{-1} (98.7% selectivity), substantially surpassing pristine TZCOF (51.6% selectivity), Co-TZCOF (88.5% selectivity), and Ni-TZCOF (85.9% selectivity) by factors of 41.2, 1.3, and 6.2, respectively. Significantly, the potential of CoNi-TZCOF for practical application was underscored by its sustained catalytic efficacy in a simulated flue gas stream (15% CO_2), affording a CO production rate of 12.9 mmol g^{-1} h^{-1} and a selectivity of 96.5%. Mechanistic investigations unveiled a synergistic donor–acceptor interaction in which the interlayer Ni sites intricately modulated the electronic structure of the intralayer Co active centers. This modulation optimized the d-band center and promoted the formation of the crucial *COOH intermediate.

This investigation establishes a sophisticated atom programming methodology for bimetallic sites within crystalline frameworks, inaugurating novel strategies for the rational design of atomically precise multi-site architectures for complex catalytic transformations.

Author contributions

J. Y. Y. conceived the project, wrote and revised the manuscript; R. Z. Z. performed the main experiments; X. C. and C. C. L. helped to conduct the experiments; J. Y. Y., P. Y. and B. T. supervised the project.

Conflicts of interest

The authors declare no competing financial interest.

Data availability

All the data supporting this article have been included in the main text and the supplementary information (SI). Supplementary information: the materials, the measurements, experimental details, and SI figures. See DOI: **https://doi.org/10.1039/d5sc08435k**.

Acknowledgements

This work was supported by the National Natural Science Foundation of China (22575139, 22134004, and 22278249), the Natural Science Foundation of Shandong Province (ZR2023MB063), the Taishan Scholars Program of Shandong Province (tsqn202306151), the Project of Shandong Provincial Center for Fundamental Science Research (YDZX2024150), and the open Fund of Hubei Provincial Key Laboratory for Preparation and Application of Catalytic Materials (202540704). This work was also supported by the Visiting Scholar Program for Faculty of Shandong Provincial Public Undergraduate Universities. The authors thanked Suzhou Deyo Bot Advanced Materials Co., Ltd (**https://www.dy-test.com/**) for support on material characterization.

Notes and references

1 E. F. Plachinski and T. P. Yoon, *Science*, 2024, **386**, 27.
2 B. Ghosh, P. Kafle, R. Mukherjee, R. Welles, D. Herndon, K. M. Nicholas, Y. Shao and I. Sharma, *Science*, 2025, **387**, 102–107.
3 Q. Cheng, D. Bhattacharya, M. Haring, H. Cao, C. Mück-Lichtenfeld and A. Studer, *Nat. Chem.*, 2024, **16**, 741–748.
4 R. Buller, S. Lutz, R. J. Kazlauskas, R. Snajdrova, J. C. Moore and U. T. Bornscheuer, *Science*, 2023, **382**, eadh8615.
5 Y. Ohki, K. Munakata, Y. Matsuoka, R. Hara, M. Kachi, K. Uchida, M. Tada, R. E. Cramer, W. M. C. Sameera, T. Takayama, Y. Sakai, S. Kuriyama, Y. Nishibayashi and K. Tanifuji, *Nature*, 2022, **607**, 86–90.
6 W. Zhou, X. Wang, W. Zhao, N. Lu, D. Cong, Z. Li, P. Han, G. Ren, L. Sun, C. Liu and W.-Q. Deng, *Nat. Commun.*, 2023, **14**, 6971.
7 A. Wagner, C. D. Sahm and E. Reisner, *Nat. Catal.*, 2020, **3**, 775–786.
8 Y. Wang, J.-X. Wei, H.-L. Tang, L.-H. Shao, L.-Z. Dong, X.-Y. Chu, Y.-X. Jiang, G.-L. Zhang, F.-M. Zhang and Y.-Q. Lan, *Nat. Commun.*, 2024, **15**, 8818.
9 Z. Li, R. Shi, J. Zhao and T. Zhang, *Nano Res.*, 2021, **14**, 4828–4832.
10 Y. Zhao, G. Chen, T. Bian, C. Zhou, G. I. N. Waterhouse, L.-Z. Wu, C.-H. Tung, L. J. Smith, D. O'Hare and T. Zhang, *Adv. Mater.*, 2015, **27**, 7824–7831.
11 X. Xiong, Y. Zhao, R. Shi, W. Yin, Y. Zhao, G. I. N. Waterhouse and T. Zhang, *Sci. Bull.*, 2020, **65**, 987–994.
12 Y. Wang, E. Chen and J. Tang, *ACS Catal.*, 2022, **12**, 7300–7316.
13 D. Liu, H. Ma, C. Zhu, F. Qiu, W. Yu, L.-L. Ma, X.-W. Wei, Y.-F. Han and G. Yuan, *J. Am. Chem. Soc.*, 2024, **146**, 2275–2285.
14 M. Liu, C.-X. Cui, S. Yang, X. Yang, X. Li, J. He, Q. Xu and G. Zeng, *Angew. Chem., Int. Ed.*, 2024, **63**, e202401750.
15 B. Su, S. Wang, W. Xing, K. Liu, S.-F. Hung, X. Chen, Y. Fang, G. Zhang, H. Zhang and X. Wang, *Angew. Chem., Int. Ed.*, 2025, **64**, e202505453.
16 I. E. Khalil, P. Das and A. Thomas, *Acc. Chem. Res.*, 2024, **57**, 3138–3150.
17 J. Yang, Z. Chen, L. Zhang and Q. Zhang, *ACS Nano*, 2024, **18**, 21804–21835.
18 M. Zhang, C. Lai, F. Xu, D. Huang, S. Liu, Y. Fu, L. Li, H. Yi, L. Qin and L. Chen, *Coord. Chem. Rev.*, 2022, **466**, 214592.
19 K. Kong, H. Zhong, F. Zhang, H. Lv, X. Li and R. Wang, *Adv. Funct. Mater.*, 2025, **35**, 2417109.
20 C. I. Yeo, Y. S. Tan, H. T. A. Awan, A. Hanan, W. P. Wong, R. Walvekar, B. H. Goh and M. Khalid, *Coord. Chem. Rev.*, 2024, **521**, 216167.
21 S. Mohata, P. Majumder and R. Banerjee, *Chem. Soc. Rev.*, 2025, **54**, 6062–6087.
22 Z.-X. Pan, S. Yang, X. Chen, J.-X. Luo, R.-Z. Zhang, P. Yang, Q. Xu and J.-Y. Yue, *Chem. Eng. J.*, 2024, **493**, 152798.
23 W. Lin, F. Lin, J. Lin, Z. Xiao, D. Yuan and Y. Wang, *J. Am. Chem. Soc.*, 2024, **146**, 16229–16236.
24 S. Li, C. Gao, H. Yu, Y. Wang, S. Wang, W. Ding, L. Zhang and J. Yu, *Angew. Chem., Int. Ed.*, 2024, **63**, e202409925.
25 K. Cui, Z. Zhang, C. Wang, P. Lyu, X. Tang and Y. Xu, *Angew. Chem., Int. Ed.*, 2024, **63**, e202407298.
26 X. Lan, H. Li, Y. Liu, Y. Zhang, T. Zhang and Y. Chen, *Angew. Chem., Int. Ed.*, 2024, **63**, e202407092.
27 K. Cheng, S. Kong, J. Wang, Q. Wang, S. Yuan, P.-Z. Li and Y. Zhao, *Angew. Chem., Int. Ed.*, 2025, **64**, e202504772.
28 Q. Xu, J. Han, F. Tian, X. Zhao, J. Rong, J. Zhang, P. She, J.-S. Qin and H. Rao, *J. Am. Chem. Soc.*, 2025, **147**, 10587–10597.
29 K. Sun, Y. Huang, Q. Wang, W. Zhao, X. Zheng, J. Jiang and H.-L. Jiang, *J. Am. Chem. Soc.*, 2024, **146**, 3241–3249.

30 L. Zou, Z.-A. Chen, D.-H. Si, S.-L. Yang, W.-Q. Gao, K. Wang, Y.-B. Huang and R. Cao, *Angew. Chem., Int. Ed.*, 2023, **62**, e202309820.
31 C. Jia, Q. Wang, J. Yang, K. Ye, X. Li, W. Zhong, H. Shen, E. Sharman, Y. Luo and J. Jiang, *ACS Catal.*, 2022, **12**, 3420–3429.
32 Y. Ying, X. Luo, J. Qiao and H. Huang, *Adv. Funct. Mater.*, 2021, **31**, 2007423.
33 G. Yang, M. Fan, Q. Liang, X. He, W. Zhang and T. Asefa, *Angew. Chem., Int. Ed.*, 2025, **64**, e202421168.
34 H. Dong, L. Fang, K.-X. Chen, J.-X. Wei, J.-X. Li, X. Qiao, Y. Wang, F.-M. Zhang and Y.-Q. Lan, *Angew. Chem., Int. Ed.*, 2025, **64**, e202414287.
35 Z. Wang, X. Jin, C. Zhu, Y. Liu, H. Tan, R. Ku, Y. Zhang, L. Zhou, Z. Liu, S.-J. Hwang and H. J. Fan, *Adv. Mater.*, 2021, **33**, 2104718.
36 X.-Y. Dong, H. Chen, S. Wang, R.-Y. Zou, S.-Q. Zang and J. Cai, *Adv. Mater.*, 2025, **37**, 2413710.
37 J. Zhao, J. Liu, Z. Li, K. Wang, R. Shi, P. Wang, Q. Wang, G. I. N. Waterhouse, X. Wen and T. Zhang, *Nat. Commun.*, 2023, **14**, 1909.
38 Y. Li, H. Wang, X. Yang, T. O'Carroll and G. Wu, *Angew. Chem., Int. Ed.*, 2024, **63**, e202317884.
39 L. Wang, J. Li, S. Ji, Y. Xiong and D. Wang, *Energy Environ. Sci.*, 2024, **17**, 8482–8528.
40 M. Zhou, Z. Wang, A. Mei, Z. Yang, W. Chen, S. Ou, S. Wang, K. Chen, P. Reiss, K. Qi, J. Ma and Y. Liu, *Nat. Commun.*, 2023, **14**, 2473.
41 W. Xie, Y. Liu, X. Zhang, H. Yan, X.-H. Liu, X. Zhang, Q. Zhao and H. Huang, *Angew. Chem., Int. Ed.*, 2024, **63**, e202314384.
42 N. Wang, Y. Zhang, C. Shao, L. Yuan, M. Sun, H. Wang, S. Zhang and J. Wang, *Adv. Funct. Mater.*, 2025, **35**, 2423683.
43 X.-Y. Dong, F.-Q. Yan, Q.-Y. Wang, P.-F. Feng, R.-Y. Zou, S. Wang and S.-Q. Zang, *J. Mater. Chem. A*, 2023, **11**, 15732–15738.
44 R. Xu, D.-H. Si, S.-S. Zhao, Q.-J. Wu, X.-S. Wang, T.-F. Liu, H. Zhao, R. Cao and Y.-B. Huang, *J. Am. Chem. Soc.*, 2023, **145**, 8261–8270.
45 W. Geng, Y.-Y. Xiong, C.-X. Chen, S. Ning, Z. Xiong, S. Deng, Y. Tan, X. Song, M. Pan, M. Mayor and C.-Y. Su, *Angew. Chem., Int. Ed.*, 2025, **64**, e202505546.
46 Y. Yang, C.-C. Chen, M. C. Scott, C. Ophus, R. Xu, A. Pryor, L. Wu, F. Sun, W. Theis, J. Zhou, M. Eisenbach, P. R. C. Kent, R. F. Sabirianov, H. Zeng, P. Ercius and J. Miao, *Nature*, 2017, **542**, 75–79.
47 Y. Wang, T. Sun, T. Zheng, X. Ding, P. Zhang, Q. Xu, T. Li, S. Zhang, K. Wang, L. Xu and J. Jiang, *ACS Mater. Lett.*, 2024, **6**, 140–152.
48 H. Lv, P. Li, X. Li, A. Chen, R. Sa, H. Zhu and R. Wang, *Chem. Eng. J.*, 2023, **451**, 138745.
49 Q. Li, J. Wang, Y. Zhang, L. Ricardez-Sandoval, G. Bai and X. Lan, *ACS Appl. Mater. Interfaces*, 2021, **13**, 39291–39303.
50 D. Wang, X. Li, L.-L. Zheng, L.-M. Qin, S. Li, P. Ye, Y. Li and J.-P. Zou, *Nanoscale*, 2018, **10**, 19509–19516.
51 G. Wen, Q. Peng, C. Yuan, J. He and X. Hou, *Nanoscale*, 2025, **17**, 322–332.
52 Q. Guan, L.-L. Zhou and Y.-B. Dong, *Chem. Soc. Rev.*, 2022, **51**, 6307–6416.
53 W.-K. Han, Y. Liu, X. Yan and Z.-G. Gu, *Mater. Chem. Front.*, 2023, **7**, 2995–3010.
54 H. Shen, T. Peppel, J. Strunk and Z. Sun, *Sol. RRL*, 2020, **4**, 1900546.
55 X.-R. Tian, X.-L. Jiang, S.-L. Hou, Z.-H. Jiao, J. Han and B. Zhao, *Angew. Chem., Int. Ed.*, 2022, **61**, e202200123.
56 T. Zheng, X. Ding, T. Sun, X. Yang, X. Wang, X. Zhou, P. Zhang, B. Yu, Y. Wang, Q. Xu, L. Xu, D. Wang and J. Jiang, *Small*, 2024, **20**, 2307743.
57 M. Bonchio, J. Bonin, O. Ishitani, T.-B. Lu, T. Morikawa, A. J. Morris, E. Reisner, D. Sarkar, F. M. Toma and M. Robert, *Nat. Catal.*, 2023, **6**, 657–665.
58 Z. Ma, H. Yin, P. Lyu and Y. Xu, *Adv. Energy Mater.*, 2024, **14**, 2401619.
59 S. Jiao, X. Fu and H. Huang, *Adv. Funct. Mater.*, 2022, **32**, 2107651.
60 Z. Wang, J. Huang, L. Wang, Y. Liu, W. Liu, S. Zhao and Z.-Q. Liu, *Angew. Chem., Int. Ed.*, 2022, **61**, e202114696.
61 A. Vasileff, X. Zhi, C. Xu, L. Ge, Y. Jiao, Y. Zheng and S.-Z. Qiao, *ACS Catal.*, 2019, **9**, 9411–9417.